Exploring the limits of the self-consistent Born approximation for inelastic electronic transport

William Lee, Nicola Jean, and Stefano Sanvito*
School of Physics and CRANN, Trinity College, Dublin 2, Ireland

(Received 21 April 2008; revised manuscript received 21 December 2008; published 24 February 2009)

The nonequilibrium Green's function formalism is today the standard computational method for describing elastic transport in molecular devices. This can be extended to include inelastic scattering by the so-called self-consistent Born approximation (SCBA), where the interaction of the electrons with the vibrations of the molecule is assumed to be weak and it is treated perturbatively. The validity of such assumption and therefore of the SCBA is difficult to establish with certainty. In this work we explore the limitations of the SCBA by using a simple tight-binding model with the electron-phonon coupling strength α chosen as a free parameter. As model devices we consider Au monatomic chains and a H_2 molecule sandwiched between Pt electrodes. In both cases, our self-consistent calculations demonstrate a breakdown of the SCBA for large α and we identify a weak and a strong-coupling regime. For weak coupling our SCBA results compare closely with those obtained with exact scattering theory. However in the strong-coupling regime large deviations are found. In particular we demonstrate that there is a critical coupling strength, characteristic of the materials system, beyond which multiple self-consistent solutions can be found depending on the initial conditions in the simulation. These are entirely due to the large contribution of the Hartree self-energy and completely disappear when this is neglected. We attribute this feature to the breakdown of the perturbative expansion leading to the SCBA.

DOI: 10.1103/PhysRevB.79.085120 PACS number(s): 71.38.−k

I. INTRODUCTION

Central to the field of molecular electronics are phenomena involving the interaction between the electron current and the internal degrees of freedom of the molecule investigated. In scanning tunneling microscopy (STM) (Refs. 1–3), the molecular vibrational modes (phonons) have been exploited to desorb or to move a molecule on a surface, paving the way for phonon-assisted surface chemistry. At the same time, STM inelastic tunneling spectroscopy uses the fingerprints of vibrations in the *I-V* curve to probe the orientation and/or to identity molecules on surfaces.[4–7] Switching devices exploiting phonons have also been reported.[8]

Broadly speaking, in molecular devices, phonons are important for two reasons. First, they play a role in transport[9,10] by opening new conductance channels through which the itinerant electrons can propagate and by suppressing the transmission of purely elastic channels.[11] More dramatically, for large electron-phonon (e-p) coupling, the charge carriers become quasiparticles consisting of coupled electrons and phonons.[12] Second, from a technological point of view, phonons limit the efficiency of molecular devices because of energy dissipation. This causes heating, power loss, and instability.

Transport experiments at the nanoscale are difficult to interpret since the atomically precise device geometry is rarely known. Therefore, one usually relies on atomistic simulation techniques in order to understand the results. For elastic transport, when electron-phonon interaction is not considered and the electron-electron interaction is treated at the mean-field level, methods of note for predicting the current flowing through devices include the nonequilibrium Green's function formalism (NEGF) (Refs. 13–17) and scattering theory (ST).[12,18–20] Some of these methods have been adapted to include electron-phonon interaction, notably an extension of scattering theory [exact scattering theory (EST)] (Refs. 11 and 21–23) and the self-consistent Born approximation (SCBA) (Refs. 24 and 25) within the NEGF formalism. In addition, time-dependent methods for describing correlated electron-ion dynamics have been recently proposed.[26]

The focus of this paper is the SCBA. This is attractive from a practical point of view since it has moderate computational requirements and it has been used extensively for calculating transport properties of a number of different material systems.[24,25] However, it is a perturbative approach appropriate only for weak e-p coupling. As the e-p coupling strength increases, the SCBA will eventually breakdown; however it is unclear whether such breakdown is either sharp or smooth with the e-p coupling strength. Our work explores this question in detail. In particular, we investigate electron transport as a function of the electron-phonon coupling across the critical coupling for which the SCBA fails.

Our main result is that there is a critical coupling strength, characteristic of the device under investigation, beyond which multiple self-consistent solutions can be found depending on the initial conditions in the simulation. These are not related to the dependence of different polaronic solutions to the orbital occupation,[27,28] a feature that was recently suggested as possible mechanism of hysteresis in *I-V* curves,[29–31] but it is simply due to the breakdown of the SCBA. Interestingly, when one neglects the Hartree part of the e-p self-energy, the problem remains singled value and shows little evidence of breakdown.

The paper is organized as follows. We begin by presenting the NEGF formalism for a two-probe device[32,33] and by recalling the foundations of the SCBA. We then consider a one-dimensional (1D) tight-binding model where the e-p interaction in the scattering region is described by the Su-Schrieffer-Heeger (SSH) (Refs. 34 and 35) Hamiltonian. The parameters for the model Hamiltonian are chosen for mimicking two systems which have been studied experimentally:

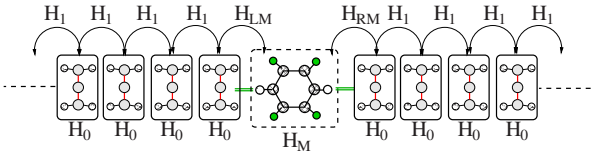

FIG. 1. (Color online) Schematic representation of a system composed of two semi-infinite leads and a scattering region (rectangular dashed box). The matrices H_0 and H_1 describe the lead principal layers, H_M describes the scattering region, and H_{LM} and H_{RM} the interaction between the scattering region and the last principal layers of the leads.

H_2 molecules sandwiched between Pt electrodes (H_2-Pt) (Refs. 9 and 36) and Au monatomic chains[10] comprising R atoms (RC's). The parameters for H_2-Pt are the same as those used by Jean and Sanvito,[11] who previously employed EST to describe phononic effects. We will then compare the SCBA results with those obtained by EST over a range of different e-p couplings in order to understand the limitation of the two methods.

II. METHODOLOGY

A. Nonequilibrium Green's function formalism

A two-probe device consists of two crystalline electrodes attached on either side of a scattering region, which is in general a collection of atoms breaking the electrodes translational symmetry. The leads are also charge reservoirs, so that the device may be viewed as two charge reservoirs bridged by the central region. Thermodynamically we characterize the left-hand side (L) and right-hand side (R) leads by defining their chemical potentials μ_L and μ_R. If $\mu_L=\mu_R$, equilibrium is established and no current flows. When $\mu_L \neq \mu_R$ the system is dragged out of equilibrium and net charge will move from the reservoir with the higher chemical potential across the central region to the reservoir of lower chemical potential in an attempt to re-establish equilibrium. If a battery is attached to the two reservoirs keeping $\mu_L - \mu_R = eV$ (V is the bias and e is the electron charge), the system cannot return to equilibrium and will eventually reach a steady state with a constant current flow.

At the Hamiltonian level, the problem can be formulated by using a basis set comprising a linear combination of atomic orbitals (LCAOs). It is convenient to write the Hamiltonian of the semi-infinite periodic leads in terms of principal layers (PLs).[32,37] These are cells that repeat periodically and constructed in such a way that the interaction between PLs extend only to nearest neighbors (see Fig. 1). Thus the $N \times N$ matrices H_1 and H_0 describe, respectively, the interactions between PLs and within a PL. The scattering region in general is described by M basis functions. The $M \times M$ matrix H_M describes its internal interaction, while the matrices H_{LM} ($N \times M$) and H_{RM} ($M \times N$) contains the interaction between the PLs of the leads adjacent to the scattering region and the scattering region itself. The entire system is thus described by the infinite tridiagonal Hamiltonian $\mathcal{H}$,

$$\mathcal{H} = \begin{pmatrix} \ddots & & & & & & & & & & \\ & 0 & H_{-1} & H_0 & H_1 & 0 & & & & & \\ & & 0 & H_{-1} & H_0 & H_{LM} & 0 & & & & \\ & & & 0 & H_{ML} & H_M & H_{MR} & 0 & & & \\ & & & & 0 & H_{RM} & H_0 & H_1 & 0 & & \\ & & & & & 0 & H_{-1} & H_0 & H_1 & 0 & \\ & & & & & & & & & & \ddots \end{pmatrix}.$$

Time-reversal symmetry sets $H_{-1}=H_1^\dagger$, $H_{ML}=H_{LM}^\dagger$, and $H_{MR}=H_{RM}^\dagger$. The retarded Green's function $\mathcal{G}^R$ associated to the entire system (leads plus scattering region) is defined as[38]

$$[\omega' \mathcal{I} - \mathcal{H}]\mathcal{G}^R(\omega) = \mathcal{I}, \tag{1}$$

where $\omega' = \lim_{\delta \to 0^+}(\omega + i\delta)$, ω is the energy and $\mathcal{I}$ is the infinite-dimensional identity matrix.

For transport calculations, however, one does not need the Green's function of the entire system but only that relative to the scattering region G_M in the presence of the leads. This can be written as[39]

$$G_M(\omega) = [\omega' I_M - H_M - \Sigma_L(\omega) - \Sigma_R(\omega)]^{-1}, \tag{2}$$

where the presence of the leads has been accounted via the introduction of the self-energies for the left- and right-hand side leads $\Sigma_L(\omega)$ and $\Sigma_R(\omega)$. I_M is the $M \times M$ identity matrix. The self-energies are $M \times M$ matrices defined as

$$\Sigma_L = H_{ML} g_L H_{LM}, \quad \Sigma_R = H_{MR} g_R H_{RM}, \tag{3}$$

where $g_L(\omega)$ and $g_R(\omega)$ are the retarded *surface* Green's functions of the leads, namely, the retarded Green's functions of the isolated semi-infinite leads evaluated at the PLs adjacent to the scattering region. These are calculated by considering the retarded Green's function of the corresponding infinite system (periodic) and by applying appropriate boundary conditions.[20,40] External bias voltage is introduced under the assumption that the leads are good metals maintaining local charge neutrality. The effect of a bias is therefore only that of shifting rigidly in energy of the leads electronic structure, so that

$$\Sigma_{L/R}(\omega, V) = \Sigma_{L/R}(\omega \pm eV/2, 0). \tag{4}$$

We now proceed to evaluate the nonequilibrium charge density in the scattering region and the two-probe current by using the NEGF scheme.[37] The lesser ($<$) and greater ($>$) Green's functions $G_M^{\lessgtr}(\omega)$ are defined as

$$G_M^{\lessgtr}(\omega) = G_M(\omega)\Sigma^{\lessgtr}(\omega)G_M^\dagger(\omega), \tag{5}$$

with self-energies

$$\Sigma^{\lessgtr}(\omega) = \sum_{\alpha=L,R} \Sigma_\alpha^{\lessgtr}(\omega), \tag{6}$$

$$\Sigma_\alpha^{<}(\omega) = i n_F^\alpha(\omega)\Gamma_\alpha(\omega), \tag{7}$$

$$\Sigma_\alpha^>(\omega) = i[n_F^\alpha(\omega) - 1]\Gamma_\alpha(\omega). \tag{8}$$

Here $n_F^\alpha(\omega)=n_F(\omega-\mu_\alpha)$ is the Fermi function evaluated at $\omega-\mu_\alpha$ and temperature T, $\mu_\alpha=E_F\pm eV/2$ with E_F is the leads Fermi energy, and we have introduced the coupling matrix for the α lead ($\alpha=L/R$),

$$\Gamma_\alpha(\omega,V) = i[\Sigma_\alpha(\omega,V) - \Sigma_\alpha^\dagger(\omega,V)]. \tag{9}$$

The nonequilibrium charge-density matrix for the scattering region is

$$\rho = \frac{1}{2\pi i}\int_{-\infty}^{\infty} d\omega' G_M^<(\omega'). \tag{10}$$

If H_M has a functional dependence on ρ, Eqs. (2) and (10) can be solved self-consistently. The net current flowing through the device is then

$$J_{\rm unp}(V) = \frac{2e}{h}\int_{-\infty}^{\infty} {\rm d}\omega\ {\rm Tr}[\Gamma_L G_M^\dagger \Gamma_R G_M](n_F^L - n_F^R), \tag{11}$$

where the subscript "unp" stands for "unperturbed," meaning that no e-p interaction is included. The term $T(\omega,V)={\rm Tr}[\Gamma_L G_M^\dagger \Gamma_R G_M]$ is the standard Landauer-Büttiker transmission coefficient; although in this case it is explicitly bias dependent. The conductance G in the linear-response limit is

$$G = \frac{2e^2}{h}T(E_F,0), \tag{12}$$

while more generally at a given bias V, one has

$$G(V) = \left.\frac{dJ_{\rm unp}}{dV}\right|_V. \tag{13}$$

B. Self-consistent Born approximation

We now discuss the main concepts associated with introducing e-p scattering into the NEGF transport scheme. In general, inelastic scattering produces loss of phase coherence, similarly to what happens when an electron is absorbed by a reservoir. In fact one may think of inelastic processes as resulting from the coupling of the scattering region to a "fictitious" charge reservoir[41] that does not exchange a net current. Thus e-p interaction can be introduced via a self-energy $\Sigma_{\rm ph}(\omega)$ and the retarded Green's function becomes

$$G_M(\omega) = [\omega' I_M - H_M - \Sigma_L(\omega) - \Sigma_R(\omega) - \Sigma_{\rm ph}(\omega)]^{-1}. \tag{14}$$

The exact form for $\Sigma_{\rm ph}(\omega)$ is unknown, however, convenient approximations can be derived from the perturbative expansion over the e-p coupling strength.[16,24,25,33,42] In this work, we consider the SCBA where only the Hartree and Fock diagrams of the perturbative expansion are retained (see Fig. 2). This is equivalent to evaluating the first-order diagrams at the interacting electronic Green's function. Thus the phonon self-energy reads as

$$\Sigma_{\rm ph}(\omega) = \Sigma^F(\omega) + \Sigma^H, \tag{15}$$

where the retarded Hartree and Fock contributions to the self-energies are, respectively,[33,44]

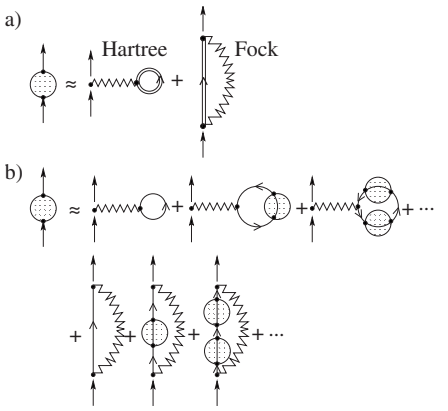

FIG. 2. Diagrammatic representation of the Hartree-Fock approximation. (a) The self-consistent proper self-energy (the shaded circle) is obtained from the first-order Hartree-Fock diagrams evaluated using the interacting Green's function (double line). This is equivalent to resumming all the diagrams (Ref. 43) in (b).

$$\Sigma^H = i\sum_\lambda \frac{4}{\Omega_\lambda}\int_{-\infty}^{\infty}\frac{d\omega'}{2\pi}M^\lambda\ {\rm Tr}[G_M^<(\omega')M^\lambda], \tag{16}$$

$$\Sigma^F(\omega) = \sum_\lambda\left[\frac{1}{2}[\Sigma_\lambda^>(\omega) - \Sigma_\lambda^<(\omega)] - \frac{i}{2}\mathcal{H}_{\omega'}\{\Sigma_\lambda^>(\omega') - \Sigma_\lambda^<(\omega')\}(\omega)\right]. \tag{17}$$

In Eq. (17) $\mathcal{H}_{\omega'}$ is the Hilbert transform,

$$\mathcal{H}_x\{f(x)\}(y) = \frac{1}{\pi}\mathcal{P}\int_{-\infty}^{\infty} dx\frac{f(x)}{x-y}, \tag{18}$$

and $\mathcal{P}$ stands for the principal part of the integral. The phonon energy and e-p coupling matrix for a particular mode λ are, respectively, Ω_λ and M^λ. Finally the e-p lesser and greater self-energies are given by

$$\Sigma^{F\lessgtr}(\omega) = \sum_\lambda \Sigma_\lambda^{\lessgtr}(\omega), \tag{19}$$

$$\Sigma_\lambda^{\lessgtr}(\omega) = M^\lambda[(N_\lambda+1)G_M^{\lessgtr}(\omega\pm\Omega_\lambda) + N_\lambda G_M^{\lessgtr}(\omega\mp\Omega_\lambda)]M^\lambda, \tag{20}$$

which is simply a sum of the self-energies over all the possible modes λ. The occupancy of each phonon mode is N_λ.

We assume that the phonons are in thermal equilibrium with a bath, so that for a given temperature N_λ is simply the Bose-Einstein distribution $N_\lambda=(e^{\Omega_\lambda/K_BT}-1)^{-1}$, with K_B the Boltzman's constant. From Eq. (20) we note that the lesser (greater) self-energy contains contributions from two scattering processes: electrons with energy $\omega-\Omega_\lambda$ may absorb (emit) a phonon and/or electrons with energy $\omega+\Omega_\lambda$ may emit (absorb) a phonon of energy Ω_λ. When $T\sim 0$, electrons may only emit phonons since $N_\lambda\sim 0$, i.e., no phonons are present in the scattering region provided that the phonon

lifetime is much smaller than that of the electrons. The total lesser self-energy of Eq. (6) must be adjusted to include the phonon self-energy,

$$\Sigma^{\lessgtr}(\omega) = \sum_{\alpha=L,R} \Sigma^{\alpha\lessgtr}(\omega) + \Sigma^{\lessgtr}_{\rm ph}(\omega), \tag{21}$$

and $G^{\lessgtr}(\omega)$ from Eq. (5) are now evaluated using the perturbed Green's function and self-energy from Eqs. (14) and (21). The general expression for the interacting (including e-p coupling) current[45] through lead β may be written as the sum of elastic and inelastic contributions

$$J^{\beta}(V) = J^{\beta}_{\rm el}(V) + J^{\beta}_{\rm inel}(V),$$

where

$$J^{\beta}_{\rm el} = \frac{2e}{h}\int_{-\infty}^{\infty} {\rm d}\omega\ {\rm Tr}[\Gamma_{\beta} G_M \Gamma_{\alpha} G_M^{\dagger}](n_F^{\beta} - n_F^{\alpha}) \tag{22}$$

and

$$J^{\beta}_{\rm inel} = \frac{2e}{h}\int_{-\infty}^{\infty} d\omega\ {\rm Tr}[\Sigma^{<}_{\beta} G_M \Sigma^{>}_{\rm ph} G_M^{\dagger} - \Sigma^{>}_{\beta} G_M \Sigma^{<}_{\rm ph} G_M^{\dagger}]. \tag{23}$$

III. NUMERICAL METHOD

A. Model Hamiltonian and coupling matrices M^{λ}

The systems under investigation are 1D linear atomic chains described by an *s*-orbital nearest-neighbor tight-binding model (see Fig. 3). The scattering region comprises of R atoms plus one PL (one atom) from each lead, so that it contains $M=R+2$ orbitals. Henceforth we refer to this system as RC. Furthermore, we assume that the two leads are identical. The matrices H_0, H_1 for a 1D tight-binding model reduce to *c*-numbers: $\epsilon_L = H_0$ and $\gamma_L = H_1$, where ϵ_L, γ_L are the lead onsite energy and hopping parameter, respectively. The leads' Hamiltonians thus read as

$$\mathcal{H}_L = \epsilon_L \sum_{i=-\infty}^{-1} c_i^{\dagger} c_i + \gamma_L \sum_{i=-\infty}^{-2} [c_i^{\dagger} c_{i+1} + c_{i+1}^{\dagger} c_i], \tag{24}$$

$$\mathcal{H}_R = \epsilon_L \sum_{i=R+2}^{\infty} c_i^{\dagger} c_i + \gamma_L \sum_{i=R+1}^{\infty} [c_i^{\dagger} c_{i+1} + c_{i+1}^{\dagger} c_i], \tag{25}$$

where $\{c_i^{\dagger}, c_i\}$ are the electronic creation and annihilation operators at site i. The interaction Hamiltonian between the leads and the scattering region are

$$\mathcal{H}_{LM} = \gamma_{LM}[c_{-1}^{\dagger} c_0 + c_0^{\dagger} c_{-1}], \tag{26}$$

$$\mathcal{H}_{\rm RM} = \gamma_{\rm LM}[c_{R+1}^{\dagger} c_{R+2} + c_{R+2}^{\dagger} c_{R+1}], \tag{27}$$

where for our setup $\gamma_{LM} = \gamma_L$.

For a 1D system, the lead self-energies are analytical

$$\Sigma^{R}_{L(R)}(\omega) = \Delta(\omega) - i\frac{\Gamma(\omega)}{2}, \tag{28}$$

where

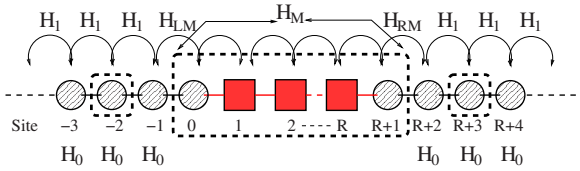

FIG. 3. (Color online) Schematic diagram of the simple monatomic systems considered here. It is composed of two semi-infinite leads and a scattering region. The scattering region is marked with a dashed rectangle. Inelastic scattering is effective only in the scattering region.

$$\Delta(\omega) = \Gamma_0 \begin{cases} x, & |x| \le 1 \\ x - \sqrt{x^2 - 1} & |x| > 1, \end{cases} \tag{29}$$

$$\Gamma(\omega) = -2\Gamma_0 \theta(1 - |x|)(\sqrt{1 - x^2}),$$

$$\Gamma_0 = \frac{\gamma_{LM}^2}{\gamma_L}, \quad x = \frac{(\omega - \epsilon_L)}{2\gamma_L}. \tag{30}$$

Finally, e-p interaction is included into the scattering region in the form of an SSH Hamiltonian,[34,35] comprising three terms

$$H_M = H_e + H_{\rm ep} + H_{\rm ph}, \tag{31}$$

with

$$H_e = \sum_{i=0}^{R+1} \epsilon_i c_i^{\dagger} c_i + \sum_{i \ne j} \gamma_{ij}^0 (c_i^{\dagger} c_j + c_j^{\dagger} c_i), \tag{32}$$

$$H_{\rm ph} = \sum_{\lambda=1}^{\lambda_{\max}} \left(b_{\lambda}^{\dagger} b_{\lambda} + \frac{1}{2} \right) \hbar \omega_{\lambda}, \tag{33}$$

$$H_{\rm ep} = \sum_{\lambda=1}^{\lambda_{\max}} \sum_{i \ne j} M_{ij}^{\lambda} (b_{\lambda}^{\dagger} + b_{\lambda})(c_i^{\dagger} c_j + c_j^{\dagger} c_i). \tag{34}$$

H_e is the electronic Hamiltonian of the scattering region with onsite energies ϵ_i and the unperturbed hopping parameters γ_{ij}^0 (we assume $\gamma_{ij}^0 = 0$ for $j \ne i \pm 1$). $H_{\rm ph}$ is the noninteracting phonons Hamiltonian written in terms of the phononic creation and annihilation operators $\{b_{\lambda}^{\dagger}, b_{\lambda}\}$ and the phonon energies $\Omega_{\lambda} = \hbar\omega_{\lambda}$, with the index λ running over all the modes.[46] The final term $H_{\rm ep}$ is the Hamiltonian describing the e-p interaction within the scattering region. The details of such interaction are included in the e-p coupling matrices M_{ij}^{λ}.

In order to calculate the matrices M_{ij}^{λ} and the longitudinal phonon frequencies, we consider a simple nearest-neighbors elastic model[23,24,47] in which

$$M_{ij}^{\lambda} = \alpha_{ij} \left\{ \frac{e_{\lambda}^{i}}{\sqrt{m_i}} - \frac{e_{\lambda}^{j}}{\sqrt{m_j}} \right\} \sqrt{\frac{\hbar}{2\omega_{\lambda}}}. \tag{35}$$

In Eq. (35) the orthonormal vectors e_{λ} represent the ionic displacement associated to each mode λ, m_i is the mass of the atom at site i, and the constants α_{ij} are the e-p coupling parameters. These latter are defined as the first-order coeffi-

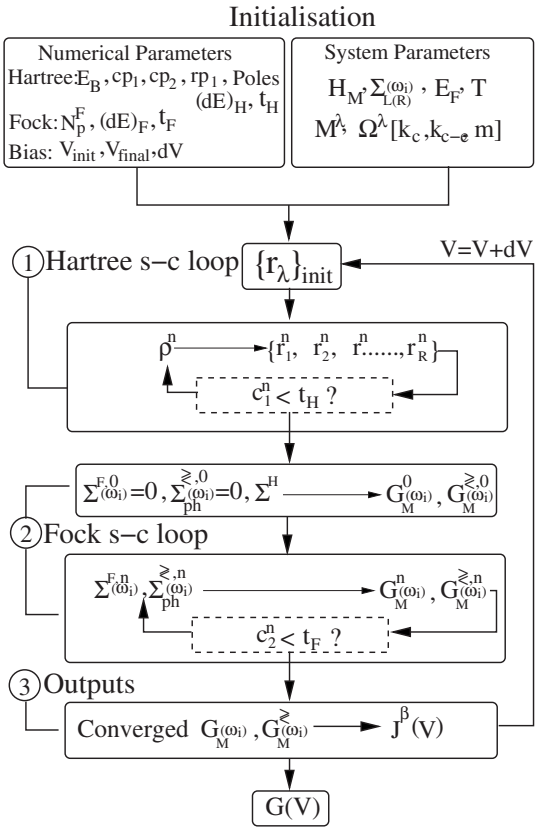

FIG. 4. Scheme of our numerical procedure for self-consistency.

cient of the expansion of the tight-binding hopping parameter γ_{ij} about the atomic equilibrium positions,

$$\gamma_{ij} = \gamma_{ij}^0 + \alpha_{ij}(u_i - u_j), \tag{36}$$

where u_i is the displacement vector of the atom at site i. From Eq. (36) it follows that $\alpha_{ij}=-\alpha_{ji}$. In the nearest-neighbor approximation, the interaction is restricted to electrons moving between sites i and $i\pm1$. Finally, we note that the eigenvectors e_λ are real. This implies that the matrices M_{ij}^λ are real and symmetric with nonzero matrix elements for $i=i\pm1$, so that M_{ij}^λ has a tridiagonal form for longitudinal phonons. We note that although it is possible to calculate the coupling parameters α_{ij} using first-principles electronic structure methods, here we set $\alpha_{ij}=\alpha$ and α is taken as a free parameter.

B. Numerical integration and self consistency

The flowchart in Fig. 4 outlines the numerical procedure used to calculate the interacting current $J^\beta(V)$ and the differential conductance $G(V)$. Each simulation can be partitioned into three steps. The first two consist of two self-consistent loops which calculate the phonon self-energies Σ^H and Σ^F, respectively. These are used in the third step to evaluate $J^\beta(V)$ by using the Eqs. (22) and (23).

Let us now discuss the three steps in some details. We start by writing Σ^H as an explicit function of the density matrix ρ,

$$\Sigma^H(\rho) = -4\sum_\lambda \mathrm{Tr}\left[\rho\frac{M^\lambda}{\Omega_\lambda}\right]M^\lambda, \tag{37}$$

where we assume that all the elements of $G_M^<$ are integrable. Σ^H is thus nothing but a weighted sum of the matrices M^λ. This can be written in the form

$$\Sigma^H = \sum_{\lambda=1}^{M} r_\lambda R^\lambda, \tag{38}$$

where the ratio matrices R^λ and their weighting coefficients r_λ are given by

$$R^\lambda = \frac{|\gamma^0|_{\min}}{|M^\lambda|_{\max}}M^\lambda. \tag{39}$$

$$r_\lambda = -\frac{4|M^\lambda|_{\max}}{\Omega^\lambda|\gamma^0|_{\min}}\sum_{i=1}^{M-1} R_{i,i+1}^\lambda(\rho_{i,i+1}+\rho_{i+1,i}). \tag{40}$$

For a given mode λ, the largest matrix elements of the matrix M^λ is denoted as $|M^\lambda|_{\max}$. $|\gamma^0|_{\min}$ is the smallest among the hopping parameters of the unperturbed system (no e-p coupling), which, by construction, is equal to $|R^\lambda|_{\max}$. The matrices R^λ are independent of the e-p coupling α and simply reflect the symmetry of the specific phonon mode considered. Thus r_λ measures the maximum fractional modification of the elements γ_{ij}^0 in the electronic Hamiltonian as the result of e-p coupling.

The first self-consistent loop of Fig. 4 begins by choosing the initial values for the weighting coefficients $\{r_\lambda\}_{\text{init}}=\{r_1^0, r_2^0, \ldots, r_R^0\}$, which are used to construct the density matrix at the first iteration ρ^1. Then both $\{r_\lambda\}$ and ρ are varied until the convergence condition,

$$c_1^n = \sum_\lambda \left(\frac{|r_\lambda^n - r_\lambda^{n-1}|}{|r_\lambda^{n-1}|}\right) < t_H \tag{41}$$

is met for the chosen tolerance t_H. The density matrix ρ is obtained by integrating $G^<$ as in Eq. (10). In order to perform this integral, we first take $\Sigma^F=0$ under the assumption that this has little effect of the convergence of ρ (first self-consistent loop). Following previous works,[32,48] we write $\rho=\rho_{\text{eq}}+\rho_V$, where

$$\rho_{\text{eq}} = -\frac{1}{\pi}\int_{-\infty}^{\infty} d\omega\ \mathrm{Im}[G_M]n_F^L, \tag{42}$$

and

$$\rho_V = \frac{1}{2\pi}\int_{-\infty}^{\infty} d\omega G_M\Gamma_R G_M^\dagger(n_F^R - n_F^L). \tag{43}$$

At equilibrium ($\mu_L=\mu_R=\mu$), one has $\rho=\rho_{\text{eq}}$.

As shown in Fig. 5(b), the integral of ρ_V [Eq. (43)] is along the real axis and it is bound between the chemical potentials μ_L and μ_R. This is carried out over a numerical grid of sufficient fineness $(dE)_H$. The calculation of ρ_{eq} involves an unbound integral. This is performed over a coarse grid in the complex plane using a contour integral method,[49] since G_M is analytical[50] and smooth in the imaginary energy

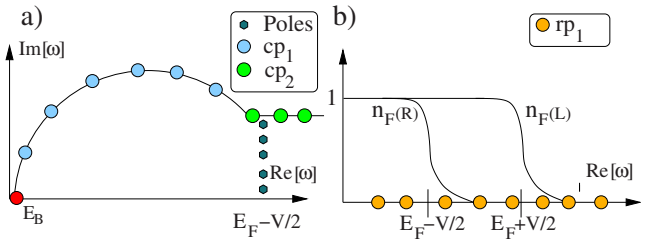

FIG. 5. (Color online) Schematic representation of the integrals in Eqs. (42) and (43), respectively. In (a) the number of grid points along the circular path (cp_1) and the path in the complex plane parallel to the real axis (cp_2) must be chosen, as well as the poles in the Fermi functions. In (b) the integration of ρ_V is bound between $E_F+eV/2$ and $E_F-eV/2$ by the Fermi functions. rp_1 is the number of points of the real axis energy grid.

plane. As shown in Fig. 5(a), a number of numerical parameters must be chosen. First the lower limit of integration E_B must lie below the lowest-lying molecular states and below the lowest electrode bands. Second, the poles of the Fermi functions (Matsubara frequencies) which lie within the contour must be taken into account. The integration is then performed by using Gaussian quadrature.[51]

The second self-consistent loop begins by calculating $\{G_M^0, G^{\gtrless,0}\}$ using Eq. (14), where the converged Σ^H from the first loop is used and $\Sigma^F=0$. We then proceed to iterate $\{\Sigma^F, \Sigma_{\rm ph}^{\gtrless}\}$ and $\{G_M, G^{\gtrless}\}$ until a second convergence condition is met

$$c_2^n = \frac{1}{N_p^F}\max\{|[G_M^n(\omega_i) - G_M^{n-1}(\omega_i)]|\} < t_F. \tag{44}$$

Note that the condition is over the largest of the matrix elements and runs over the N_p^F energy points ω_i of the entire grid. Note also that the tolerance used t_F is in general different to that used for the Hartree term. The Hilbert transform required for calculating the imaginary part of Σ^F [Eq. (17)] is done by using a convolution method combined with a fast Fourier transform algorithm.[24] In order to avoid end-point corrections, we choose a grid of sufficient range while the grid fineness $(dE)_F$ must be sufficiently fine to resolve phononic features which lie in the meV range.

Table I shows the numerical and system parameters used in our simulations. The parameters for the H_2-Pt junctions are identical to those used by Jean[11] within the EST treatment of phonons. This set produces the same unperturbed $G(0)\sim.97G_0$. The spring constants and masses are chosen to give longitudinal phonon modes of energies 63 (CM mode) and 432 meV, respectively, while the ratio matrices for these two modes are

$$R^1 = \begin{pmatrix} 0 & 3.2 & 0 & 0 \\ 3.2 & 0 & 0 & 0 \\ 0 & 0 & 0 & -3.2 \\ 0 & 0 & -3.2 & 0 \end{pmatrix} \tag{45}$$

and

TABLE I. Parameters used to simulate the H_2-Pt junctions and Au RC's. The parameter K_c is to the spring constant between the atoms in the chain, while K_{c-e} is to the spring constant between the molecule and the electrodes. The Fock grid and real Hartree grid are symmetric about E_F.

System parameter	H_2-Pt	Au RC	
Symbol	Value	Value	Units
E_F	0.00	0.00	eV
ϵ_M (molecule)	−6.0	0.00	eV
ϵ_L (leads)	0.00	0.00	eV
γ_L (leads)	5	−1.00	eV
γ_M (molecule)	6.0	−1.00	eV
γ_{LM}	3.2	−1.00	eV
T	4.0	4.0	K
m (atomic mass)	1	197	amu
K_c	21.82	2.00	eV/Å^2
K_{c-e}	0.91	1.00	eV/Å^2
Numerical parameter	**Value**	**Value**	**Units**
$[V_{\rm ini}, V_{\rm final}]$ (Bias range)	[0,200]	[0,31]	meV
Number of bias points	250	120	
$(dE)_F$ (Fock)	0.1	0.1	meV
N_p^F (Fock)	12600	12600	
rp_1, (Hartree)	4000	4000	
$(dE)_H$ (Hartree)	0.1061	0.0215	meV
cp_1 (Hartree)	400	200	
cp_2 (Hartree)	400	200	
E_B (Hartree)	−28.0	−5.0	eV
Poles (Hartree)	80	80	
t_F (tolerance)	9×10^{-8}	9×10^{-8}	eV^{-1}
t_H (tolerance)	1×10^{-8}	1×10^{-6}	

$$R^2 = \begin{pmatrix} 0 & 1.6 & 0 & 0 \\ 1.6 & 0 & -3.2 & 0 \\ 0 & -3.2 & 0 & 1.6 \\ 0 & 0 & -1.6 & 0 \end{pmatrix}. \tag{46}$$

The e-p coupling α remains a free parameter.

The parameters for the Au RC's match closely those used by Frederiksen of Ref. 24. The atoms in the leads are chosen as identical to the atoms in the scattering region, thus that a single onsite energy and hopping parameter characterize the electronic Hamiltonian. These parameters and the equilibrium potential $\mu_{\rm eq}$ are chosen so that the differential conductance for the unperturbed system is $G_0=2e^2/h$ (perfect transmission).

IV. RESULTS: H_2-Pt JUNCTIONS

A. Self-consistent simulations

The self-consistent $G(V)$ in the range 0–110 meV for α ranging between 0 and 3.1 eV/Å are presented in Fig. 6. For

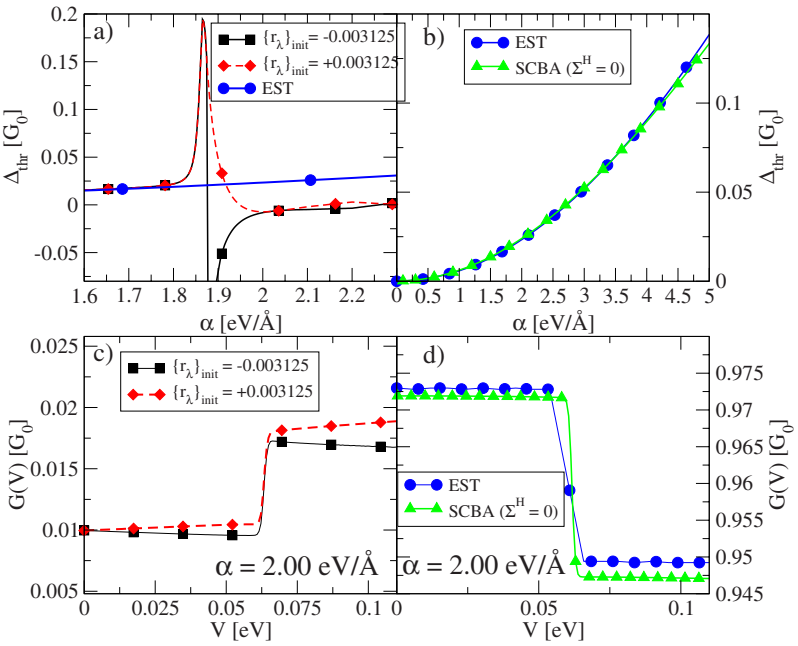

FIG. 6. (Color online) Differential conductance and conductance drop at threshold for the H_2-Pt junctions—V_{thr} is taken at 68.5 meV. Results obtained using the SCBA including both Hartree and Fock terms (HF-SCBA) are given for the different initial conditions (panels a and c). In panels (b) and (d) we also show results obtained by setting $\Sigma^H=0$. In this second case Δ_{thr} and $G(V)$ agree well with the EST (Ref. 11) up to $\alpha \approx 4.0$ eV/Å. The HF-SCBA disagrees with the EST at a considerably lower $\alpha \approx 1.8$ eV/Å. Above such a coupling strength $G(V)$ depends on the initial conditions.

this system the characteristic signature of e-p interaction is a drop in the conductance at a threshhold voltage V_{thr}. This signals the onset of inelastic electron processes involving the emission of phonons with energies $\Omega \approx eV_{thr}$. We quantify this effect by defining the conductance drop (in units of G_0),

$$\Delta_{thr} = G(0) - G(V_{thr}). \tag{47}$$

Numerical simulations are carried out in two different ways. First, we follow the exact numerical procedure of Fig. 4 ("HF-SCBA"), but we run simulations starting with different initial conditions, namely, $\{r_\lambda\}_{init}=+3.125\cdot10^{-3}$ and $\{r_\lambda\}_{init}=-3.125\cdot10^{-3}$. In Fig. 6(a) Δ_{thr} is plotted versus α demonstrating good agreement between the HF-SCBA and EST for low α. However, the two methods disagree for α beyond $\alpha_{crit} \sim 1.8$ eV/Å. Δ_{thr} peaks sharply above α_{crit}, beyond which it becomes dependent on the initial condition $\{r_\lambda\}_{init}$. This last situation is shown in Fig. 6(c) for $\alpha=2.0$ eV/Å, where two different $G(V)$ curves are predicted for different $\{r_\lambda\}_{init}$ and a low-bias conductance of 0.0125 G_0 is observed in stark disagreement with the unperturbed value of $\sim 0.97 G_0$. Note that for $\alpha=\alpha_{crit}$ the e-p coupling constant entering the perturbative expansion of the SCBA $[M^\lambda]$ is rather large reaching the value of 240 meV for the first mode. This suggests that the development of multiple solutions in this case originates from a breakdown of the SCBA.

Since the Hartree self-consistent loop is performed before the Fock one, the dependence on the initial conditions suggests that Σ^H may be responsible for the behavior observed for $\alpha > \alpha_{crit}$. Stronger evidence to support this hypothesis is provided in Figs. 6(b) and 6(d), where the results for our second set of simulations in which Σ^H is set to zero are presented (Fock-only SCBA or in short F-SCBA). Figure 6(b) shows good agreement between the F-SCBA and the EST to the much higher coupling of $\alpha \sim 4.0$ eV/Å. Moreover there is no evidence of any α_{crit}. This is confirmed by the $G(V)$ curve obtained for $\alpha=2.0$ eV/Å and presented in Fig. 6(d).

In order to have a better insight into the relationship between the EST and the SCBA, we have looked in detail at the elastic transmission coefficient (the dominant one in this case) calculated with both EST and the SCBA, as a function of the el-ph coupling strength α. This is plotted in Fig. 7 for the EST [panel (a)], the SCBA [panel (b)], and the Fock-only SCBA [panel (c)]. In the case of EST and Fock-only SCBA, we investigate α both larger and smaller than α_{crit}, while we consider only $\alpha < \alpha_{crit}$ in the case of the SCBA.

Interestingly, $T(\omega)$ for the EST and the Fock-only SCBA remain rather similar for α on both sides of α_{crit}, in sharp contrast to what happens when the Hartree self-energy is included. This means—at least for our particular model system—that the scattering properties are well described at the Fock level, even in the case of strong e-p coupling. How-

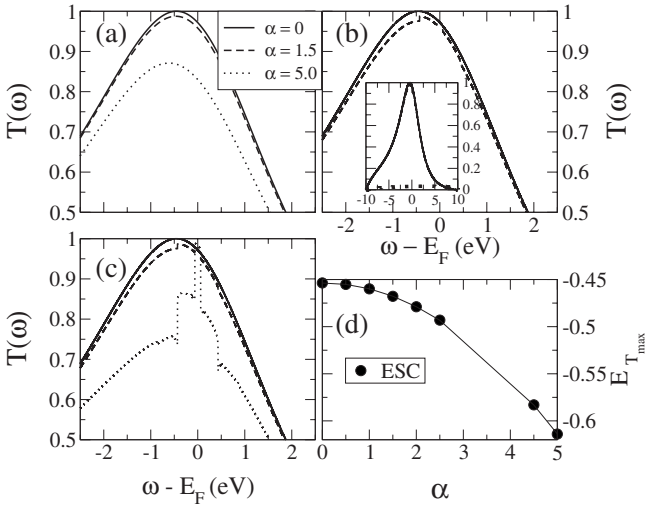

FIG. 7. Zero-bias elastic transmission coefficient for H_2-Pt as a function of energy for different e-p coupling strengths α: (a) EST, (b) SCBA, and (c) Fock-only SCBA. In panel (d) we trace the maximum of $T(E)$ calculated from EST as a function of α.

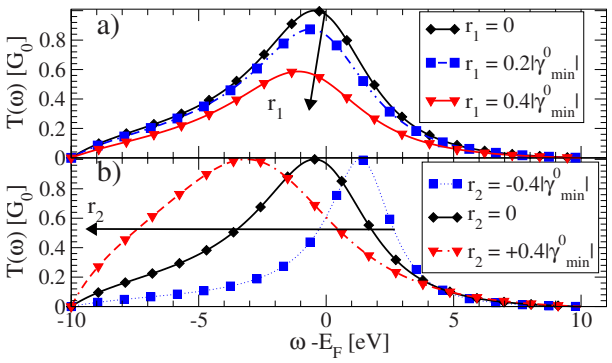

FIG. 8. (Color online) Transmission coefficients calculated using the Green's function G_M^λ of Eq. (48) for (a) $\lambda=1$ and (b) $\lambda=2$. The matrices R^1 and R^2 are fixed and a range of values for r_λ has been chosen.

ever, it is important to remark that neglecting the Hartree term means essentially to neglect the polarization response of the molecule. Since this can be the crucial factor in determining the scattering potential, both F-SCBA and EST in general can say little about the actual scattering properties of the system. Thus EST cannot be used as benchmark for the validity of the SCBA. As a final note, we observe that the maximum of $T(E)$ calculated with EST shifts to lower energies as a function of α. The shift however is in the opposite direction to what is expected from the polarization of the H_2 molecule[27] and described in the SCBA by the Hartree self-energy.

B. Contribution from the individual modes

We now analyze the origin the breakdown of the HF-SCBA. For $V \ll V_{\text{thr}}$ the inelastic current J_{inel} is strongly suppressed by Pauli exclusion principle. At low temperature ($T=4.0$ K), we can approximate the Fermi distributions in J_{el} by step functions to obtain

$$J^\beta(V) \simeq \frac{2e}{h}\int_{\mu_L}^{\mu_R} T(\omega)d\omega.$$

We can now easily probe the contribution of the Hartree term to the conductance by considering the test Green's function,

$$G_M^\lambda(\omega) = [\omega' I_M - H_M - \Sigma_L - \Sigma_R - r_\lambda R^\lambda]^{-1}. \quad (48)$$

This is used to evaluate the transmission coefficient at $V=0$ and it is useful to understand the influence of the individual modes λ over the transmission. In Fig. 8 we show $T(\omega)$ as a function of r_λ for the two longitudinal modes available in the H_2-Pt system (see Fig. 9). In the case of the rigid translational mode [$\lambda=1$ and Fig. 8(a)] $T(\omega)$ is reduced in the region around E_F as $|r_1|$ increases. However, the general shape of $T(\omega)$ is little affected. This is somehow expected from the shape of the matrix R^1 [Eq. (45)], which indicates that mode 1 causes simply a change in the hopping parameters γ_{12}^0 and γ_{34}^0 connecting the molecule to the leads. Importantly when γ_{12}^0 is increased, γ_{34}^0 is reduced by the same amount and viceversa. Moreover there is a symmetry $r_1 \to -r_1$.

The results for the symmetric mode $\lambda=2$ are presented in Fig. 8(b). This time the peak in transmission is shifted in energy either to the left or to the right depending on the sign of r_2. When shifted to the left, the peak is broadened while a shift to the right narrows it. In either case the transmission around E_F is reduced.

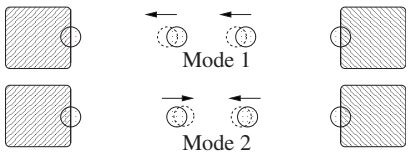

FIG. 9. The longitudinal vibration modes of H_2-Pt junctions. The $\lambda=1$ mode of energy 63 meV is the rigid translational of the H_2 center of mass, while the $\lambda=2$ mode is the symmetric mode of energy 432 meV. The atoms of the leads are fixed.

From Figs. 6(c), 8(a), and 8(b) one can conclude that the deviation of the zero-bias differential conductance from its unperturbed (no e-p interaction) value is a measure of the magnitude of the e-p perturbation. We define this deviation as

$$\Delta G = G_0 - G(0) \cong G_0 - T(E_F), \quad (49)$$

where the last equality is valid for $T \to 0$. Figures 10(a) and 10(b) show the estimated deviation (in units of G_0) versus the weighting coefficients r_λ. The maximum deviation $\Delta G=1$ occurs when the chain actually breaks as for mode 1 and $r_1=1$. As expected, the curve in Fig. 10(a) for mode 1 is symmetric about 0, while Fig. 10(b) for mode 2 is not.

C. Discussion of the self-consistent results

We finally reanalyze our self-consistent results in light of the discussion in Sec. IV B. Figures 11(a) and 11(b) show the self-consistently calculated r_λ as a function of α for $V=0$, while Fig. 11(c) shows ΔG as defined in Eq. (49). The critical point $\alpha_{\text{crit}} \sim 1.8$ eV/Å marks a sharp transition in the behavior of the weighting coefficients. This is evident in the abrupt change in magnitude and behavior of ΔG [in Fig.

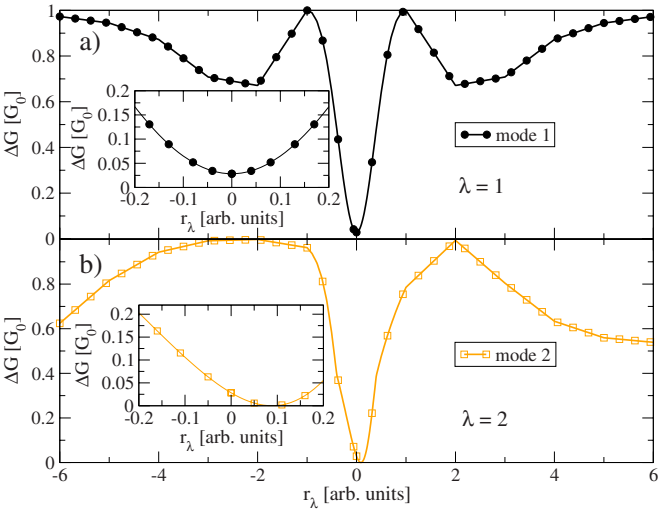

FIG. 10. (Color online) Estimate of the deviation ΔG caused by an individual mode λ as a function of r_λ. The insets show the region of small perturbation.

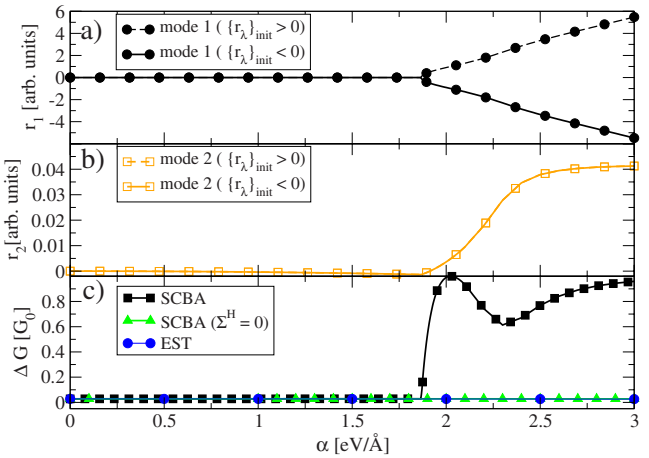

FIG. 11. (Color online) Converged self-consistent values of r_λ and deviation ΔG [Eq. (49)] as a function of the e-p coupling strength α for $V=0$. A transition is apparent at $\alpha = 1.865 \pm 0.005$ eV/Å for the HF-SCBA. Panels (a) and (b) show, respectively, r_1 and r_2 for the HF-SCBA for different initial conditions, while in (c) results for the F-SCBA and EST are also included.

11(c)]. In fact while for $\alpha < \alpha_{crit}$ the HF-SCBA agrees well with the EST; the two differ sharply as soon as $\alpha > \alpha_{crit}$. Going into more detail, we note that r_1 is identically zero ($\sim 10^{-14}$) for $\alpha < \alpha_{crit}$, while r_2 is small and negative. Importantly both r_1 and r_2 are independent of $\{r_\lambda\}_{init}$. By contrast, for $\alpha > \alpha_{crit}$, r_2 remains independent of $\{r_\lambda\}_{init}$ but this is not the case of r_1. In fact we obtain a strong dependence over the initial conditions with positive (negative) r_1 for positive (negative) $\{r_\lambda\}_{init}$. Importantly none of these features is found in the case when we neglect the Hartree self-energy.

Since $|r_1|$ is 2 orders of magnitude larger than $|r_2|$, it will largely determine Σ^H. As Fig. 11(a) shows, r_1 varies roughly linearly with α above α_{crit}; therefore the self-consistent ΔG follows the estimated curve of Fig. 10(a) in this region of α. The magnitude of r_1 for $\alpha > \alpha_{crit}$ suggests that the interaction with phonons becomes a strong perturbation of the electronic system. We define the region $\alpha < \alpha_{crit}$ as the weak-coupling regime and the region $\alpha > \alpha_{crit}$ as the strong-coupling regime.

Figure 11 adequately explains the causes of the massive reduction of $G(V)$ with respect to its unperturbed value observed in Fig. 6(c) at $V=0$. Notably, as Fig. 6(a) shows, Δ_{thr} calculated with the HF-SCBA starts deviating from the EST result for $\alpha \simeq 1.75$ eV/Å, i.e., at a value lower that $\alpha_{crit} = 1.865 \pm 0.005$ eV/Å calculated for $V=0$. This seems to suggest that the critical value of α for the breakdown of the HF-SCBA somehow depends on the bias. Moreover, at finite bias α_{crit} is characterized by a peak in $\Delta_{thr}(\alpha)$ for positive $\{r\}_{init}$ and by a discontinuity for negative $\{r\}_{init}$ [see Fig. 6(a)].

In order to explore the onset of the breakdown of the SCBA at finite bias in Fig. 12(a), we present $G(V)$ for $\alpha = 1.84$ eV/Å, i.e., just below the zero-bias critical value. In addition, in Fig. 12(b) we plot the dominant coefficient r_1 for a small range of α about α_{crit} at three different bias, $V=0$, $V=0.1$, and $V=0.2$ V. A clear result from Fig. 12(a) is that the presence of Σ^H introduces a reduction of $G(V)$ with bias not present at $V=0$. For $\alpha < \alpha_{crit}$ Fig. 12(b) shows that $|r_1|$ is a function of bias whose value increases as the bias increases. The difference between r_1 at $V=0$ and at finite V explains the deviation below α_{crit} and also the origin of the peak above it.

The discontinuity in Δ_{thr} for $\{r_\lambda\}_{init} > 0$ of Fig. 6(a) is explained by the discontinuities observed in r_1 [Fig. 12(b)] and in the current $J^\beta(V)$ [Fig. 12(c)]. In fact at $V=0$, r_1 is single valued as long as $\alpha < \alpha_{crit}$. For $\alpha > \alpha_{crit}$ instead $r_1(\alpha)$ has a parabolic shape symmetric about $r_1=0$: the $\{r_\lambda\}_{init} < 0$ solution traces out the lower arm of the parabola and the $\{r_\lambda\}_{init} > 0$ solution follows the upper arm as α increases. For $V > 0$, it is seen that the two solutions for r_1 are identical and

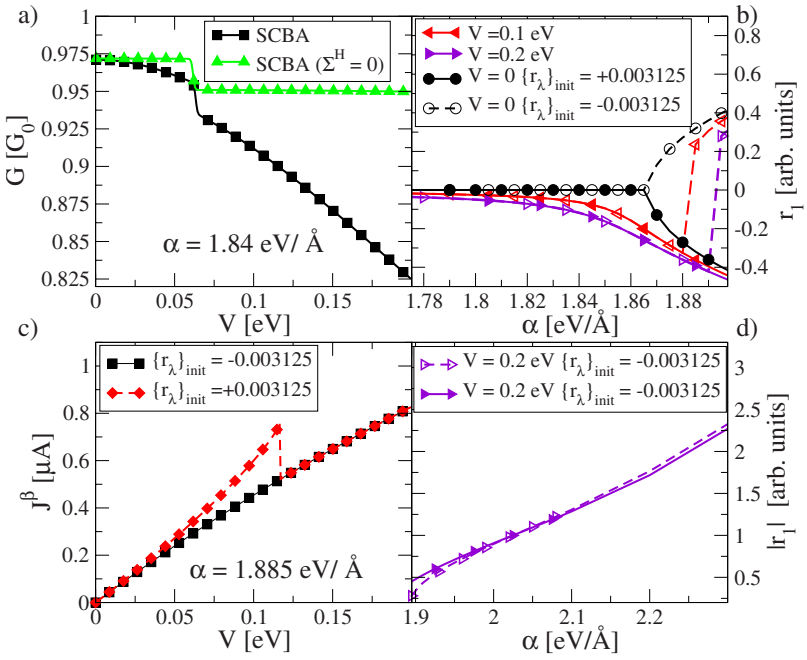

FIG. 12. (Color online) Behavior of the SCBA in the region above and below the zero-bias α_{crit}. For $\alpha < \alpha_{crit}$, $G(V)$ for the HF-SCBA and F-SCBA are compared in panel (a), showing that the contribution arising from Σ^H is bias dependent. For $\alpha > \alpha_{crit}$, J^β calculated with the HF-SCBA is presented in (c) for two different initial conditions. In panel (b) the functional dependence of the weighting coefficient r_1 upon bias is investigated for a range of coupling strengths and bias. Finally, in panel (d) we show the magnitude $|r_1|$ obtained from two HF-SCBA simulations with different initial conditions and $\alpha > \alpha_{crit}$.

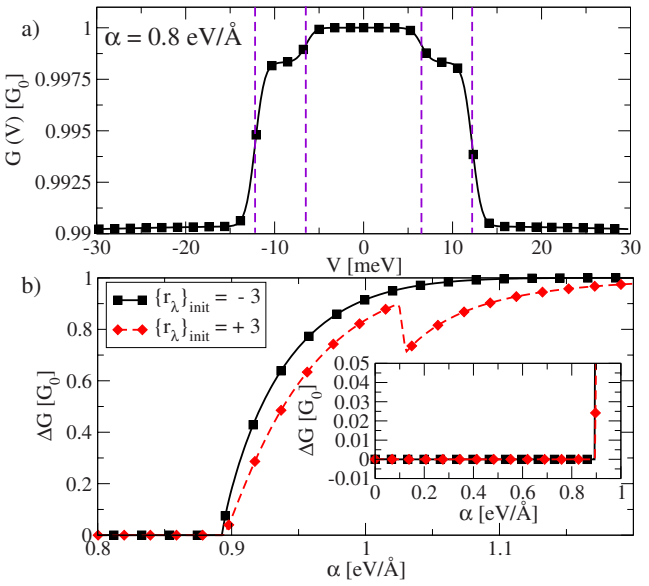

FIG. 13. (Color online) $G(V)$ for the 4C illustrating the onset of inelastic processes at threshhold voltages. These are associated to the symmetric modes of energy $\Omega_2=6.5$ meV and $\Omega_4=12.2$ meV. The rigid and antisymmetric modes of energies, respectively, $\Omega_1=3.1$ meV and $\Omega_3=9.8$ meV have no effect for chains comprising an even number of atoms. No overall shift in $G(V)$ is observed as α lies below the critical coupling α_{crit} which is clearly determined from the inset in panel b.

asymptotically approach the lower arm of the $V=0$ curve from below for $\alpha > \alpha_{\mathrm{crit}}$. However, as α is further increased, the $\{r_\lambda\}_{\mathrm{init}} > 0$ solution jumps discontinuously above zero and then asymptotically approaches the upper arm again from below.

The discontinuity in $r_1(\alpha, V)$ is determined by both the bias and the initial conditions. Generally, it is found that such discontinuity occurs for lower bias first; r_1 jumps discontinuously for $V=0.1$ V before it does for $V=0.2$ V. This explains the behavior of the $\{r_\lambda\}_{\mathrm{init}}=+3.125\cdot 10^{-3}$ solution for $J^\beta(V)$ in Fig. 12(c) which leads to a peak in its derivative (the conductance $G(V)$) and explains the discontinuity of Δ_{thr}.

We note that after the discontinuity in r_1 for $V>0$, the two solutions are no longer symmetric about $r_1=0$ and do not converge to the $V=0$ solutions of either arm until $\alpha \approx 3.0$ eV/Å. This is highlighted in Fig. 12(d) where $|r_1|$ for the two solutions is plotted in a range of α just above α_{crit} at $V=0.2$ V. Such differences explain why Δ_{thr} is not independent of the initial conditions beyond the discontinuity and also the different curves observed for $G(V)$ in Fig. 6(c).

We make a final comment about the discontinuities seen in Fig. 12(a). The value of α at which these occur is dependent on the initial conditions as mentioned already. Thus for a particular $\{r_\lambda\}_{\mathrm{init}}$ it may be possible to reach the upper solution at α_{crit} for all bias, so that r_1 has a parabolic shape for bias while being asymmetric about 0. We have not observed this and regard α_{crit} as uniquely defined for $V=0$ only.

V. RESULTS: AU CHAINS

By using the procedure outlined in Sec. III and the parameters of Table I, the HF-SCBA is used to calculate the transport of the Au RC's. In general we observe a behavior similar to that of the H_2-Pt system. For 3C, 4C, 5C, and 6C a weak-coupling regime is identified where the shift ΔG and the weighting coefficients are zero. A critical coupling strength α_{crit} for $V=0$ was discovered for each of the chains investigated with values $\alpha_{\mathrm{crit}} \approx 0.85, 0.9, 0.82, 0.83$ eV/Å, respectively, for 3C, 4C, 5C, and 6C. For weak coupling ΔG matches closely the values calculated in previous works.[24,44] As an example, in Fig. 13 we present $G(V)$ and $\Delta G(\alpha)$ for 4C. It is seen that the modes symmetric with respect to the center of the scattering region (even numbered) induce drops in $G(V)$ at threshhold voltages corresponding to the energy of the modes. In general, only the symmetric modes are active in RC's containing an even number of atoms and conversely the rigid and antisymmetric modes are active for an odd RC.

TABLE II. Mode energy Ω_λ and $|M^\lambda|_{\mathrm{max}}$ (in meV) for the four Au chains investigated. In the last column we indicate the symmetry of the specific mode: R rigid translation, S symmetric, and A antisymmetric.

Chain	Mode	Ω_λ	$\lvert M^\lambda\rvert_{\mathrm{max}}$	Type
3	1	3.6	24.5	R
3	2	7.9	22.1	S
3	3	11.6	31.3	A
4	1	3.1	23.5	R
4	2	6.5	22.8	S
4	3	9.8	29.4	A
4	4	12.2	34.1	S
5	1	2.6	18.5	R
5	2	5.5	19.8	S
5	3	8.4	19.3	A
5	4	10.9	25.1	S
5	5	12.5	26.3	A
6	1	2.3	17.0	R
6	2	4.8	19.2	S
6	3	7.3	17.5	A
6	4	9.7	22.3	S
6	5	11.5	24.1	A
6	6	12.6	25.2	S

In order to investigate the features of the breakdown of the SCBA in Table II we report the energy of the various phonon modes of the Au chains and the e-p coupling parameter $|M^\lambda|_{\mathrm{max}}$. For this latter, we present the zero-bias value at $\alpha=\alpha_{\mathrm{crit}}$. In general and for all the chains, no single mode appears to develop a particularly large e-p coupling. Therefore the breakdown of the SCBA in this case seems to be subtly driven also by the symmetry of the e-p coupling matrices. We note that, before the breakdown, symmetric (S) modes are active in reducing the conductance for even-numbered chains, while asymmetric (A) and rigid translational modes (R) are active for the odd ones (see Fig. 14). With this in mind we find that in all cases there is always an active mode with $|M^\lambda|_{\mathrm{max}} > 25$ meV at the breakdown. Note also that the condition $\max|M^\lambda| < \gamma_{LM}$ is never violated so

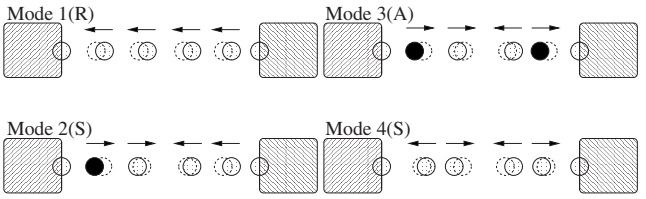

FIG. 14. Vibration modes of Au 4C. Modes 2 and 4 are symmetric modes (S) about the center of the scattering region. Mode 1 is the rigid translational mode (R) while mode 3 is antisymmetric (A). For all chains considered, the mass of the lead atoms is taken sufficiently larger than that of the chain atoms so that they do not vibrate.

that the chain remains strongly coupled to the leads.

The transition from weak to strong coupling can be appreciated for the 4C by looking at the inset of Fig. 13(b), where for $\alpha > \alpha_{\text{crit}}$ two different initial conditions lead to two different ΔG. The 6C shows the same behavior of the 4C, while the 3C and 5C show a single curve for ΔG due to the symmetry of the weighting coefficients in the strong regime. Beyond α_{crit}, for all the RC's simulated $G(V)$ is reduced to zero as α increased and the shift ΔG rises to G_0.

Finally we want to investigate further the existence of multiple solutions depending on the initial conditions in the self-consistent loops. As an example of how convergence is achieved in Fig. 15, we show the coefficient r_4 as a function of the iteration number n for the 4C plotted for a single bias $V=0.02$ V and coupling 0.902 eV/Å ($\alpha > \alpha_{\text{crit}}$). A number of simulations were run with different initial conditions. The figure indicates the existence of two stable minima: simulations which start at $\{r_\lambda\}_{\text{init}} > 0$ (dashed lines) converge to the same positive final value, while simulations initialized with $\{r_\lambda\}_{\text{init}} < 0$ converge to the same $r_4 < 0$ value. We note that the minima are not symmetric about $r_4 = 0$. The solution $r_\lambda = 0$ appears to be a minima in the weak-coupling regime but becomes unstable and evolves to a local maximum in the strong-coupling regime.

In Fig. 16 r_6 for 6C is plotted versus the number of iterations n for $\alpha > \alpha_{\text{crit}}$. This time we run different simulations in which the lower bound of the energy integration grid (EB) is changed. In particular we explore situations where EB is not below the lower band edge of the leads that for our choice of parameters lies at −2 eV (see Table I). The figure indicates

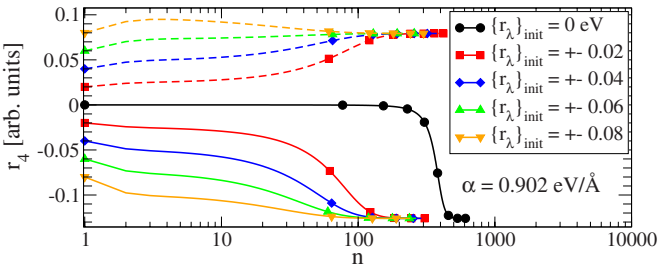

FIG. 15. (Color online) Test of the convergence of the weighting coefficient r_4 for the 4C and $\alpha > \alpha_{\text{crit}}$ using a range $\{r_\lambda\}_{\text{init}}$ where n is the number of iterations. Results for the calculations with positive starting values are indicated with dashed lines while those with negative initial values are shown with solid lines. A single negative and positive solution for the converged r_4 are found.

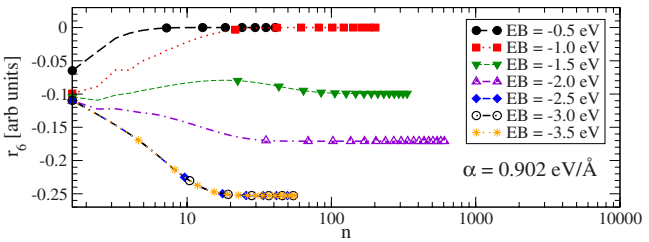

FIG. 16. (Color online) Convergence test. The zero bias r_6 for 6C is plotted versus the iteration number n for $\{r_\lambda\}_{\text{init}} = -0.09$ and $\alpha > \alpha_{\text{crit}}$. Here the lower bound for the integration of the charge density ρ (EB) is varied. The lower band edge of the leads lies at −2 eV. Clearly when EB ≥ -2 eV, r_6 does not converge fully, i.e., it depends on EB.

that if EB ≥ -1 eV r_6 converges to zero so that the sixth mode gives no contribution to Σ^H. For $-2 \leq$ EB < -1 r_6 is nonzero, however, the converged value differs for EB $= -1.5$ eV and for EB $= -2.0$ eV, i.e., it is sensitive on the grid lower bound. Finally for EB < -2.0 eV the bands of the leads are entirely included in the integral and r_6 converges to a value of approximately −0.25 eV which is independent of our choice of EB. From this simple analysis, it appears that cutting the integration grid can result in the erroneous suppression of the Hartree self-energy, i.e., in a drastic underestimate of its contribution. This produces a fortuitous suppression of the SCBA breakdown, since the agreement between SCBA and EST is usually improved when Σ^H is neglected.

Finally we test the robustness of our integration method. Figure 17 shows the transmission coefficients $T(\omega)$ for a 6C at a bias of $V=1$ mV where only the sixth mode is considered. We run two simulations. In the first case, the HF-SCBA is used with the numerical parameters taken from Table I and initial condition $\{r_6\}_{\text{init}} = -9.75 \cdot 10^{-3}$. In the second case, the integration method outlined in Sec. III B is replaced by Simpson's rule along the real axis. The integration range used is $[-3.093, 0.1]$ eV with a grid fineness $(dE)_H = 2.129 \times 10^{-5}$ eV. The Hartree self-consistent loop is started with $\{r_6\}_{\text{init}} = 0.0$ and finished when $c_1^n < t_H = 10^{-12}$ (this tolerance was also used in the first case). All other parameters of the calculations are identical in the two cases. The figure shows that the two numerical methods produce the same $T(\omega)$, specifically, in the range of applied bias shown in the inset.

VI. CONCLUSIONS

By using a simple 1D tight-binding model, we have investigated the breakdown of the SCBA as a function of the e-p coupling strength α. We have identified two regimes. In the weak-coupling regime there is a unique solution for both Σ^H and Σ^F, independently of the initial conditions. In particular, the Hartree self-energy is small and has little effect on the final conductance. In this weak-coupling regime, the characteristic conductance drops at voltages corresponding to the various phonon energies compared well with those calculated with the EST method.

As the coupling parameter α is increased beyond some critical value α_{crit}, a sharp transition to the strong-coupling

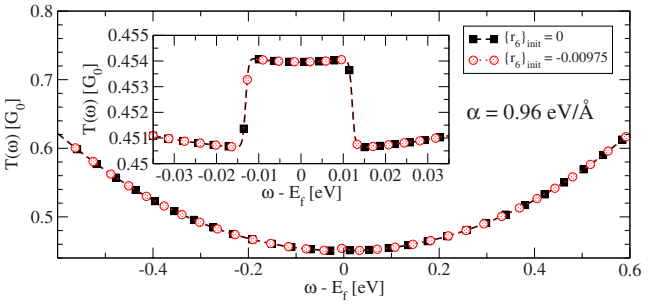

FIG. 17. (Color online) $T(\omega)$ for a 6C simulation where only the sixth mode of energy $\Omega_6=12.6$ meV is included. The curves show results obtained when Σ^H is calculated using the Simpson's rule ($\{r_6\}_{\text{init}}=0$ in the legend) or the contour method ($\{r_6\}_{\text{init}}=-0.00975$ in the legend).

regime occurs. In this limit the self-consistent Σ^H becomes unstable with respect to the initial conditions and exhibits multiple values for the same voltage. Such a behavior is not associated to the dependence of the polar response of the molecule to the level occupation,[27,28] but it simply denotes a breakdown of the SCBA. Thus, for $\alpha > \alpha_{\text{crit}}$ the electron-phonon interaction cannot be treated perturbatively. Interestingly such a breakdown is suppressed when the Hartree self-energy is neglected completely from the calculation, as sometimes done in practice. Our results show that although neglecting the Hartree self-energy is sometime valid,[52] it cannot be taken as a general prescription in quantitative calculations based on e-p parameters extracted from density-functional theory. For these, no information is available on whether or not the obtained e-p coupling strength is either below or above the critical value for the SCBA to breakdown. Therefore, strictly speaking, one rarely knows whether the SCBA is applicable.

ACKNOWLEDGMENTS

The authors acknowledge the financial support of IRCSET and Science Foundation of Ireland. They thank Ivan Rungger for all his advice and useful discussions. Calculations have been performed at the Trinity Centre for High Performance Computing (TCHPC) and at the Irish Centre for High-End Computing (ICHEC).

*sanvitos@tcd.ie

[1] J. I. Pascual, N. Lorente, Z. Song, H. Conrad, and H. P. Rust, Nature (London) **423**, 525 (2003).
[2] M. Ohara, Y. Kim, and M. Kawai, Chem. Phys. Lett. **426**, 357 (2006).
[3] T. Komeda, Y. Kim, B. N. J. Persson, and H. Ueba, Science **295**, 2055 (2002).
[4] Y. Sainoo, Y. Kim, T. Okawa, T. Komeda, H. Shigekawa, and M. Kawai, Phys. Rev. Lett. **95**, 246102 (2005).
[5] K. W. Hipps and U. Mazur, J. Phys. Chem. **97**, 7803 (1993).
[6] B. C. Stipe, M. A. Rezaei, and W. Ho, Phys. Rev. Lett. **82**, 1724 (1999).
[7] R. C. Jaklevic and J. Lambe, Phys. Rev. Lett. **17**, 1139 (1966).
[8] L. Cai, M. A. Cabassi, H. Yoon, O. M. Cabarcos, C. L. McGuiness, A. K. Flatt, D. L. Allara, J. M. Tour, and T. S. Mayer, Nano Lett. **5**, 2365 (2005).
[9] R. H. M. Smit, Y. Noat, C. Untiedt, N. D. Lang, M. C. van Hemert, and J. M. van Ruitenbeek, Nature (London) **419**, 906 (2002).
[10] N. Agrait, C. Untiedt, G. Rubio-Bollinger, and S. Vieira, Phys. Rev. Lett. **88**, 216803 (2002).
[11] N. Jean and S. Sanvito, Phys. Rev. B **73**, 094433 (2006).
[12] H. Ness and A. J. Fisher, Phys. Rev. Lett. **83**, 452 (1999).
[13] L. V. Keldysh, Sov. Phys. JETP **20**, 1018 (1965).
[14] A. R. Rocha, V. M. Garcia-Suarez, S. W. Bailey, C. J. Lambert, J. Ferrer, and S. Sanvito, Nature Mater. **4**, 335 (2005).
[15] J. Rammer and H. Smith, Rev. Mod. Phys. **58**, 323 (1986).
[16] P. Danielewicz, Ann. Phys. (N. Y.) **152**, 239 (1984).
[17] C. Caroli, R. Combescot, P. Nozieres, and D. St-James, J. Phys. C **5**, 21 (1972).
[18] M. Magoga and C. Joachim, Phys. Rev. B **57**, 1820 (1998).
[19] M. Buttiker, Y. Imry, R. Landauer, and S. Pinhas, Phys. Rev. B **31**, 6207 (1985).
[20] S. Sanvito, C. J. Lambert, J. H. Jefferson, and A. M. Bratkovsky, Phys. Rev. B **59**, 11936 (1999).
[21] J. Bonca and S. A. Trugman, Phys. Rev. Lett. **75**, 2566 (1995).
[22] K. Haule and J. Bonca, Phys. Rev. B **59**, 13087 (1999).
[23] E. G. Emberly and G. Kirczenow, Phys. Rev. B **61**, 5740 (2000).
[24] T. Frederiksen, Master's thesis, Technical University of Denmark, 2004.
[25] M. Galperin, M. A. Ratner, and A. Nitzan, J. Chem. Phys. **121**, 11965 (2004).
[26] E. J. McEniry, D. R. Bowler, D. Dundas, C. Horseld, Andrew P. Sanchez, and T. N. Todorov, J. Phys.: Condens. Matter **19**, 196201 (2007).
[27] P. Hyldgaard, S. Hershfield, J. H. Davis, and J. W. Wilkins, Ann. Phys. (N. Y.) **236**, 1 (1994).
[28] A. S. Alexandrov and N. F. Mott, *Polarons and Bipolarons* (World Scientific, Singapore, 1995).
[29] A. S. Alexandrov and A. M. Bratkovsky, Phys. Rev. B **67**, 235312 (2003).
[30] M. Galperin, M. A. Ratner, and A. Nitzan, Nano Lett. **5**, 125 (2005).
[31] M. Galperin, A. Nitzan, and M. A. Ratner, J. Phys.: Condens. Matter **20**, 374107 (2008).
[32] A. Rocha, Ph.D. thesis, Trinity College Dublin, 2007.
[33] S. Datta, *Electronic Transport in Mesoscopic Systems*, 2nd ed. (Cambridge University Press, New York, 1995).
[34] W. P. Su, J. R. Schrieffer, and A. J. Heeger, Phys. Rev. Lett. **42**, 1698 (1979).
[35] W. P. Su, J. R. Schrieffer, and A. J. Heeger, Phys. Rev. B **22**, 2099 (1980).
[36] D. Djukic, K. S. Thygesen, C. Untiedt, R. H. M. Smit, K. W. Jacobsen, and J. M. van Ruitenbeek, Phys. Rev. B **71**, 161402(R) (2005).
[37] A. R. Rocha, V. M. Garcia-Suarez, S. Bailey, C. Lambert, J.

Ferrer, and S. Sanvito, Phys. Rev. B **73**, 085414 (2006).
[38] The superscript "R" is omitted throughout the paper unless necessary.
[39] A generalization to a nonorthogonal LCAO Hamiltonian is described in Ref. 37.
[40] I. Rungger and S. Sanvito, Phys. Rev. B **78**, 035407 (2008).
[41] M. Buttiker, Phys. Rev. B **33**, 3020 (1986).
[42] H. Haug and A. P. Jauho, *Quantum Kinetics in Transport and Optics of Semiconductors* (Springer-Verlag, Berlin, 1996).
[43] A. Fetter and J. D. Walecka, *Quantum Theory of Many-Particle Systems* (Dover, New York, 2003).
[44] T. Frederiksen, N. Lorente, M. Paulsson, and M. Brandbyge, Phys. Rev. B **75**, 235441 (2007).
[45] Y. Meir and N. S. Wingreen, Phys. Rev. Lett. **68**, 2512 (1992).
[46] The two lowest-energy modes correspond to the trivial translation of the whole system and to a fixed chain with slowly oscillating electrodes. These are of no interest and have been discarded. The remaining phonon energies have been labeled in order of increasing energy such that $\lambda=1$ corresponds to the lowest-energy mode.
[47] C. Kittel, *Introduction to Solid State Physics* (Wiley, New York, 1953).
[48] M. Brandbyge, J.-L. Mozos, P. Ordejon, J. Taylor, and K. Stokbro, Phys. Rev. B **65**, 165401 (2002).
[49] A. R. Williams, P. J. Feibelman, and N. D. Lang, Phys. Rev. B **26**, 5433 (1982).
[50] J. W. Brown and R. V. Churchill, *Complex Variables and Applications*, Series in Science and Engineering, (McGraw-Hill, New York, 2003).
[51] W. H. Press, B. P. Flannery, S. A. Teukolsky, and W. T. Vetterling, *Numerical Recipes in Fortran*, 2nd ed. (Cambridge University Press, New York, 1992).
[52] T. Frederiksen, M. Paulsson, M. Brandbyge, and Antti-Pekka Jauho, Phys. Rev. B **75**, 205413 (2007).